



Research Article

<https://doi.org/10.1631/jzus.A2200030>



Three-dimensional flow field mathematical model inside the pilot stage of the deflector jet servo valve

Shuang-lu LI^{1✉}, Yao-bao YIN¹, Jiang-yang YUAN², Sheng-rong GUO²

¹School of Mechanical Engineering, Tongji University, Shanghai 201804, China

²Aviation Key Laboratory of Science and Technology on Aero Electromechanical System Integration, Aviation Industry Corporation of China, Nanjing 210061, China

Abstract: A new flow field mathematical model is proposed to describe accurately the flow field structure and calculate the static characteristics of the pilot stage in a deflector jet servo valve (DJSV). The flow field is divided into five regions, a 3D turbulent jet is adopted to describe the free jet region, and a velocity distribution expression of the jet is proposed. The jet entrainment model is put forward in the pressure recovery region to describe the coupling relationship between the pressure in the receiving chamber and the jet flow. The static characteristics, including pressure-flow characteristics, pressure characteristics, and flow characteristics of the pilot stage are obtained. The flow field structure and the static characteristics are verified by finite element analysis (FEA) and experiment, respectively, and the mathematical model results are in good agreement with the experimental and simulation results.

Key words: Deflector jet servo valve (DJSV); Pilot stage; Three-dimensional jets; Jets entrainment; Static characteristics; Mathematical model

1 Introduction

High end hydraulic components, such as the electro-hydraulic servo valve (EHSV), are widely used in hydraulic servo control systems in aerospace, nuclear power, metallurgy, and other fields (Tamburrano et al., 2018). Because of the important role of the servo valve, its structure (Zhu et al., 2018; Tamburrano et al., 2020; Zheng et al., 2021), modeling and control method (Karunanidhi and Singaperumal, 2010; Stefanski et al., 2017), static and dynamic performance and evolution (Yin et al., 2017; Liu YS et al., 2019; Liu XQ et al., 2020), and other aspects have been extensively studied. The pilot stage is the core component of the two stage EHSV, which plays an important role in converting the displacement signal into pressure and flow signals. The pilot stage of DJSV has attracted great attention in flow field modeling

(Sangiah et al., 2013; Li, 2016; Yan et al., 2019; Saha et al., 2020a), flow force (Yin et al., 2019), and cavitation (Saha et al., 2020b) due to its simple structure and excellent performance.

For the circular jet nozzle and guide groove, Li (2016) assumed that the velocity at the outlet was uniform and ignored the throttle loss of the deflector. The flow gain and pressure gain were derived from the momentum theorem and closed tube jet theory. For the rectangular jet nozzle and guide groove, Sangiah et al. (2013) assumed that the pressure at the outlet of the guide groove was equal to the supply pressure and established the hydraulic full bridge model of the pilot stage. The pressure characteristic was obtained by establishing the relationship between the hydraulic resistance and the deflector position. Yan et al. (2019) divided the flow field of the pilot stage into four regions, the flow of the jet was regarded as 2D, and the energy loss caused by the guide groove was considered. The momentum theorem was applied to the region between the deflector and the receiving chamber, and the pressure characteristic was obtained by combining it with numerical simulation results. Saha et al. (2020a) also modeled the flow field based on the 2D

✉ Shuang-lu LI, 1710765@tongji.edu.cn

Shuang-lu LI, <https://orcid.org/0000-0002-3337-0791>

Received Jan. 18, 2022; Revision accepted July 11, 2022;
Crosschecked Aug. 24, 2022

© Zhejiang University Press 2022

jets, calculated the average flow velocity at the outlet of the guide groove by using the energy conservation equation, regarded the fluid in the receiving chamber and the fluid of the secondary jets as the interaction between the jets and the piston, and obtained the pressure characteristics of the pilot stage.

In the above flow field model, the jets were simplified as uniform or 2D jets. That does not reflect the real flow structure of the pilot stage because the expansion of the jets in the direction of jet-pan thickness was ignored. For the typical pilot stage of deflector jet servo valve (DJSV), the jet nozzle and guide groove are rectangular. The flow of the jet will expand along the width and height of the jet nozzle at the same time, giving 3D flow characteristics (Sforza et al., 1966). The thinner the jet-pan, the more obvious is the influence of the expansion of the jet in the thickness direction. A large amount of the 3D jet does not enter the receiving chambers and thus causes energy loss. However, the current 2D flow field mathematical model cannot reflect that.

Aiming at the defects of the current DJSV pilot stage model and based on the theory of 3D turbulent jets and the momentum conservation theorem, a flow field model of the pilot stage which is more in line with the actual state of the flow field is established. A velocity distribution expression of the flow field is proposed. The relationship between static characteristics, especially the pressure-flow characteristics and the structure parameters, is obtained as well. We hope it is beneficial to understanding the working mechanism of the pilot stage and that it will provide the theoretical basis for structure design and optimization.

2 Mathematical model of the flow field

2.1 Working principle and flow field partition of the pilot stage

A typical pilot stage includes a jet-pan, two cover plates, and a deflector which is connected to the torque motor armature component as shown in Fig. 1. There is a V-shaped groove on the deflector. The region between the jet-pan and the cover plates forms the pilot stage's flow field, and contains a jet nozzle, a pressure outlet, and two receiving chambers. The jet nozzle and pressure outlet are connected with the oil supply port and the oil return port of the servo valve, respectively, and two receiving chambers are connected to both ends of the slide valve. When the torque motor drives the armature component to move, the deflector and guide groove deviate as well and make the fluid flow into the two receiving chambers inconsistent, resulting in different recovery pressures and driving the slide spool to move.

The flow field of the pilot stage can be divided into five regions. As shown in Fig. 2, the origin o is placed in the center of the jet nozzle, the x direction is the movement direction of the deflector, the y direction is the thickness direction of the jet-pan, and the z direction is the flow direction of the jet. There are five regions, as follows:

(1) Pressure jet region: the region before the jet nozzle (region before section 1-1). In this region, the fluid forms high-speed jets and the flow from the jet nozzle is driven by the pressure difference.

(2) Free jet region: the region from the jet nozzle to the area where the jet contacts the wall of the guide

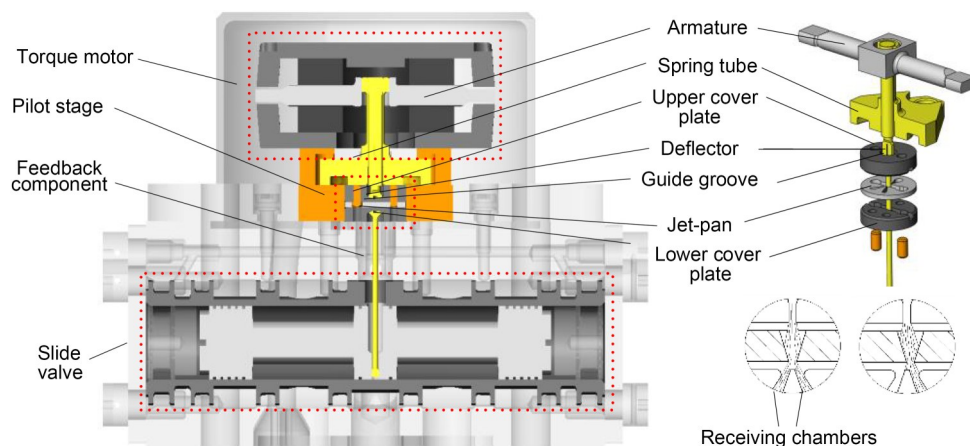


Fig. 1 Working principle of the DJSV

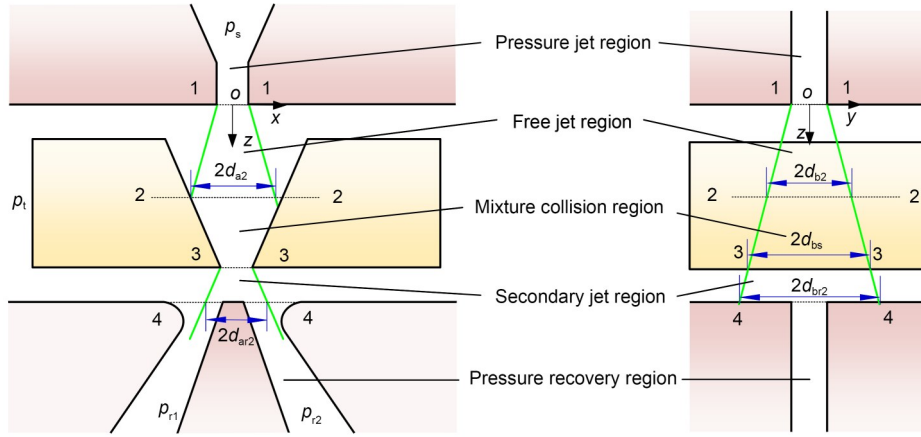


Fig. 2 Flow field partition diagram. p_{r1} and p_{r2} are the recovery pressures of the two receiving chambers

groove (the region between section 1-1 and section 2-2). In this region, the jet is unrestrained, freely expands and constantly mixes with the surrounding fluid. At section 2-2, the outer boundary of the jet along the x direction is $2d_{a2}$, and the outer boundary of the jet along the y direction is $2d_{b2}$.

(3) Mixed collision region: the region from the contact of the jet with the wall to the outlet of the guide groove (the region between section 2-2 and section 3-3). In this region, fluid collides with the wall of the deflector and causes energy loss. At section 3-3, the outer boundary of the jet along the y direction is $2d_{bs}$.

(4) Secondary jet region: the region from the outlet of the guide groove to the receiving chamber (the region between section 3-3 and section 4-4). The fluid flows from the outlet of the guide groove and then expands freely again. At section 4-4, the outer boundary of the jet along the x direction is $2d_{ar2}$, and the outer boundary of the jet along the y direction is $2d_{br2}$.

(5) Pressure recovery region: the region where the jet enters the receiving chambers and flows out of them (the region after section 4-4). The kinetic energy of the fluid converts to pressure energy again.

2.2 Pressure jet region

In the pressure jet region, the potential energy of the fluid is converted to kinetic energy. The velocity of the jet, v_1 , at the jet nozzle is as high as 200 m/s, which is a fully developed turbulence. The flow velocity at the jet nozzle can be calculated by the Bernoulli equation:

$$\frac{p_s}{\rho} = \frac{p_t}{\rho} + \frac{v_1^2}{2} + \zeta_1 \frac{v_1^2}{2}, \quad (1)$$

where ρ is the oil density, p_s is the supply pressure, p_t is the return pressure, and ζ_1 is the energy loss coefficient.

2.3 Free jet region based on 3D turbulent jets

Since the distance from the jet nozzle to the deflector is very short, the free jet region is in the potential core region of the 3D jet. There are two zones in the region; one is the constant velocity zone whose velocity is consistent with the jet nozzle, and the other is the shear layer whose velocity decreases gradually due to the mixing characteristics of the jet. Since the 3D jet is complex, the velocity distribution lacks effective mathematical expression. To facilitate calculation, as shown in Figs. 3a and 3b, the velocity distribution of the free jet region is simplified and assumed as follows:

1. The outer boundary of the jet along the x direction and y direction conforms to the linear expansion law.

2. The isovelocity line in the streamwise direction is rectangular and the velocity in the crossflow direction can be ignored (Marsters, 1981).

3. The velocity in the constant velocity zone is equal to the jet nozzle velocity and the velocity in the shear layer conforms to the cosine distribution (Squire and Truncer, 1944). The shear layer boundary along the x direction is equal to the circular jet boundary with the width of jet nozzle a as the diameter; the shear layer boundary along the y direction is equal to the circular jet boundary with the jet nozzle height b as the diameter.

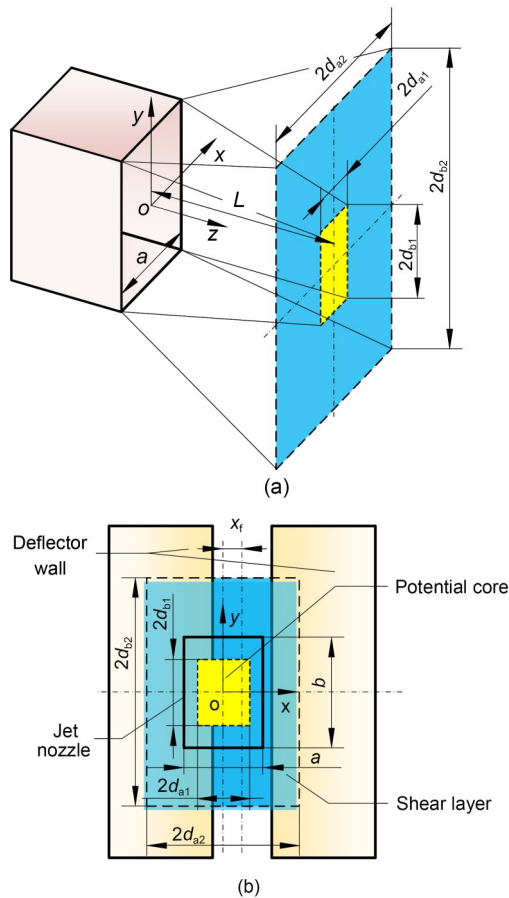


Fig. 3 Schematic diagram of the free jet region: (a) flow field structure; (b) zones in jet section

According to the above assumptions, the inner and outer boundaries of the shear layer along the x direction d_{a1} and d_{a2} are (Squire and Truncer, 1944):

$$d_{a1} = \frac{0.95a - 0.194L}{2}, \quad (2)$$

$$d_{a2} = \frac{1.07a + 0.316L}{2}, \quad (3)$$

and the inner and outer boundaries of the shear layer along the y direction d_{b1} and d_{b2} are:

$$d_{b1} = \frac{0.95b - 0.194L}{2}, \quad (4)$$

$$d_{b2} = \frac{1.07b + 0.316L}{2}, \quad (5)$$

where L is the length of the free jet, which is the distance from section 1-1 to section 2-2.

So the velocity distribution v_2 in the shear layer at section 2-2 is as follows:

$$\text{if } |y| \leq d_{b1} + k(|x| - d_{a1}), k = \frac{d_{b2} - d_{b1}}{d_{a2} - d_{a1}},$$

$$v_2(x, y) = \frac{1}{2} v_1 \left[1 - \cos \left(\frac{d_{a2} - |x|}{d_{a2} - d_{a1}} \pi \right) \right], \quad (6)$$

and in other place:

$$v_2(x, y) = \frac{1}{2} v_1 \left\{ 1 - \cos \left[\frac{d_{a2} - \left(\frac{|y| - d_{b1}}{k} + d_{a1} \right)}{d_{a2} - d_{a1}} \pi \right] \right\}. \quad (7)$$

As shown in Fig. 4, L and the structure parameters have the following geometric relationship:

$$L = L_0 - x_r \cdot \cot \theta, \quad (8)$$

where θ is the half-angle of the V-shaped guide groove, L_0 is the length of the free jet when the deflector is at zero position, x_r is the deflector displacement, and there is

$$\frac{2d_{a2} - a_n}{2 \tan \theta} + L_0 + \frac{D - d}{2} = D, \quad (9)$$

where d is the thickness of the deflector, D is the distance from the jet nozzle to the receiving chamber, and a_n is the width of the guide groove outlet.

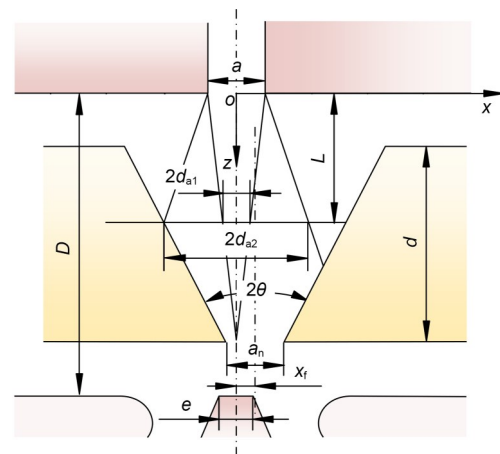


Fig. 4 Structural parameters of the jet and the pilot stage

2.4 Mixed collision region

In this region, the jet is constrained by the guide groove, the collision between fluid flow and the guide

groove results in the destruction of the 3D jet and the constant velocity zone no longer exists. Therefore, the following simplified assumptions in this region are made in combination with Fig. 5.

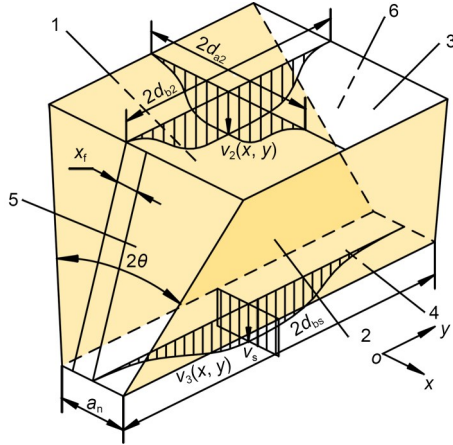


Fig. 5 Schematic diagram of the mixed jet region

1. The outer boundary of the jet along the y direction d_{bs} still conforms to the linear expansion law, but the inner boundary does not exist because the constant velocity zone disappears.

2. The velocity along the y direction at the outlet of the guide groove satisfies the cosine distribution, and the velocity distribution along the x direction is consistent.

3. The velocity in the crossflow direction is also ignored.

Based on these assumptions, the velocity distribution v_3 at section 3-3 can be obtained as follows:

$$d_{bs} = \frac{1.07b + 0.316 \frac{D+d}{2}}{2}, \quad (10)$$

$$v_3(x, y) = \frac{1}{2} v_s \left[1 - \cos \left(\frac{d_{bs} - y}{d_{bs}} \pi \right) \right], \quad (11)$$

where v_s is the maximum velocity at the outlet of the guide groove. This can be obtained by the momentum conservation theorem as follows:

Take two deflector walls of the guide groove (face No. 1 and face No. 2), sections 2-2 and 3-3 (face No. 3 and face No. 4) and the outer boundary of the jets (face No. 5 and face No. 6) as the control body, which is shown in Fig. 5. In the streamwise direction, from the law of conservation of momentum, the momentum difference between the flow entering and

leaving the control body is equal to the momentum loss in the collision between the fluid and the two deflector walls, namely:

$$J_1 - J_0 = J_{1z} + J_{2z}, \quad (12)$$

where J_1 is the momentum of the fluid entering the control body, which can be calculated by integrating the velocity at section 2-2. J_0 is the momentum of the fluid leaving the control body. J_{1z} and J_{2z} are the momentums lost by the collision between the fluid and the two deflector walls in the z direction in unit time, respectively.

As shown in Fig. 6, triangle zones on both sides are taken as the control bodies. Thus, the momentum loss in the z direction by the collision is:

$$J_{1z} = F_1 \sin \theta = J_1 \sin^2 \theta = \sin^2 \theta \iint_{A_1} \rho v_2^2(x, y) dx dy, \quad (13)$$

$$J_{2z} = F_2 \sin \theta = J_2 \sin^2 \theta = \sin^2 \theta \iint_{A_2} \rho v_2^2(x, y) dx dy, \quad (14)$$

where A_1 and A_2 are the projected areas of the two control bodies on the plane xoy . F_1 and F_2 are the flow forces acting on the two deflector walls, and J_1 and J_2 are the momentums entering the two triangular control bodies, respectively.

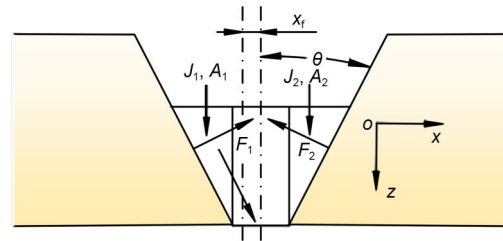


Fig. 6 Schematic diagram of the mixed jet region

2.5 Secondary jet region

In the secondary jet region, assuming that the jet boundary still conforms to the law of linear expansion as shown in Fig. 7, the inner and outer boundaries along x direction d_{ar1} and d_{ar2} and the outer boundary along y direction d_{br2} of the shear layer can be obtained as follows:

$$d_{ar1} = \frac{0.95a_n - 0.194 \frac{D-d}{2}}{2}, \quad (15)$$

$$d_{ar2} = \frac{1.07a_n + 0.316 \frac{D-d}{2}}{2}, \quad (16)$$

$$d_{br2} = \frac{1.07b + 0.316D}{2}. \quad (17)$$

The velocity distribution v_4 at section 4-4 is as follows:

inside the inner boundaries

$$v_4(x, y) = \frac{1}{2} v_s \left[1 - \cos \left(\frac{d_{ar2} - |y|}{d_{ar2}} \pi \right) \right], \quad (18)$$

outside the inner boundaries

$$v_4(x, y) = \frac{1}{4} v_s \left[1 - \cos \left(\frac{d_{ar2} - |y|}{d_{ar2}} \pi \right) \right] \left[1 - \cos \left(\frac{d_{ar2} - |x - x_f|}{d_{ar2} - d_{ar1}} \pi \right) \right]. \quad (19)$$

2.6 Pressure recovery region considering jet entrainment

As shown in Fig. 7, the pressure recovery region of the pilot stage is connected to both ends of the slide valve of the DJSV. The secondary jet enters the receiving chamber and one part is converted into a flow q_L pushing the movement of the slide spool; the other part flows out of the receiving chamber under the effect of the pressure difference between the inside and outside of the receiving chamber.

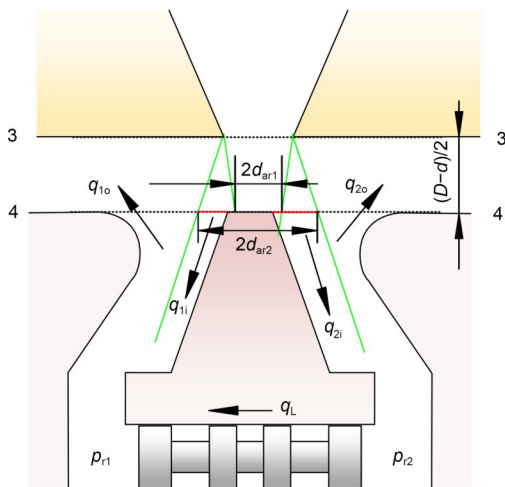


Fig. 7 Schematic diagram of secondary jet region and pressure recovery region

For the two receiving chambers, there is

$$q_L = q_{1o} - q_{1i}, \quad (20)$$

$$q_L = q_{2i} - q_{2o}, \quad (21)$$

where q_L is the load flow through the two chambers, q_{1o} and q_{2o} are the flow rates out of the chambers due to different pressures, and q_{1i} and q_{2i} are the flow rates into two chambers, respectively. As shown in Fig. 8, taking the right receiving chamber as an example, the fluid entering the receiving chamber consists of two parts, one is the jet flow received at section 4-4 q_{2s} , and the other part is the entrainment flow q_{2t} after section 4-4. The entrainment flow is decided by the jet length because of the jet expansion; the greater the jet length, the higher the entrainment flow will be.

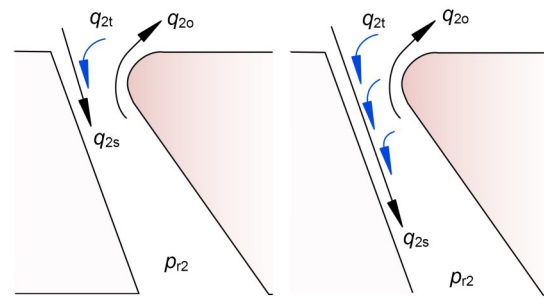


Fig. 8 Schematic diagram of jet entrainment

The jet length is related to the recovery pressure of the receiving chamber and the secondary jet flow rate; lower recovery pressure and more flow rate lead to more entrainment flow. According to the above rules, by numerical integration and the Bernoulli equation, there are

$$q_{1i} = q_{1s} + q_{1t} = \left(1 + \lambda \frac{P_s}{p_{r1} + p_a} \right) \iint_{A_{1i}} v_4(x, y) dx dy, \quad (22)$$

$$q_{2i} = q_{2s} + q_{2t} = \left(1 + \lambda \frac{P_s}{p_{r2} + p_a} \right) \iint_{A_{2i}} v_4(x, y) dx dy, \quad (23)$$

$$q_{1o} = C_d A_{1o} \sqrt{\frac{2(p_{r1} - p_i)}{\rho}}, \quad (24)$$

$$q_{2o} = C_d A_{2o} \sqrt{\frac{2(p_{r2} - p_i)}{\rho}}, \quad (25)$$

$$p_L = p_{r2} - p_{r1}, \quad (26)$$

where q_{1s} and q_{1t} are jet flows received at section 4-4 and entrainment flow of the left chamber, respectively.

p_{r1} and p_{r2} are the recovery pressures of the two receiving chambers, C_d is the flow coefficient, p_L is the load pressure difference, λ is the entrainment coefficient, and p_a is the pressure constant. λ and p_a can be obtained by fitting simulation results. A_{1i} and A_{2i} are the inflow areas of the two chambers, and A_{1o} and A_{2o} are their outflow areas. According to Fig. 9, there are

$$A_{1i} = (d_{ar2} - x_f - 0.5e) b, \tag{27}$$

$$A_{2i} = (d_{ar2} + x_f - 0.5e) b, \tag{28}$$

$$A_{1o} = L_r b - A_{1i}, \tag{29}$$

$$A_{2o} = L_r b - A_{2i}, \tag{30}$$

where e is the width of the wedge, and L_r is the length of the receiving chamber.

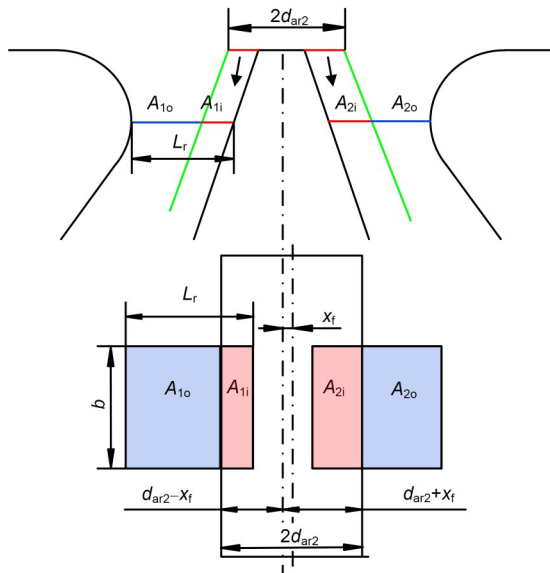


Fig. 9 Structure diagram of the receiving area

According to the above model, the relationship between the pressure and the flow of the two receiving chambers under different deflector positions can be obtained.

3 Theoretical model

The static characteristics such as pressure-flow characteristics, pressure characteristics, and flow characteristics can be calculated according to the flow field model. The calculation process for static characteristics is shown in Fig. 10. First, the jet velocity at the jet nozzle is calculated by the Bernoulli equation

according to the system pressure. Second, the jet velocity distribution at section 2-2 can be obtained according to the 3D turbulent jet flow law. Then, the velocity distribution at the outlet of the guide groove is calculated by the momentum theorem in the mixed collision region. After that, the velocity distribution at section 4-4 of the receiving chambers is obtained according to the secondary jet flow. Finally, according to the jet entrainment model, Bernoulli equation, and flow continuity theorem, the relationship between the load flow and the pressure difference of the two receiving chambers can be obtained. The main structural parameters of the pilot stage and the empirical constants are shown in Table 1.

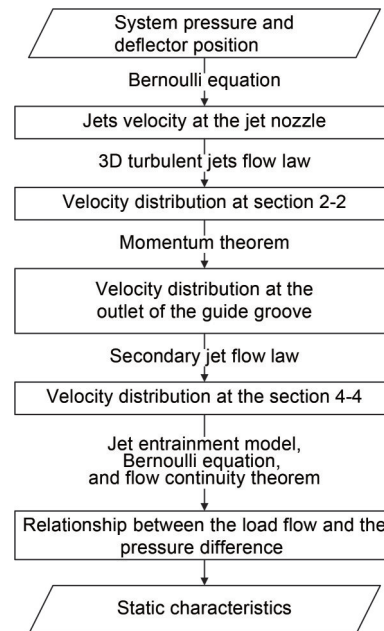


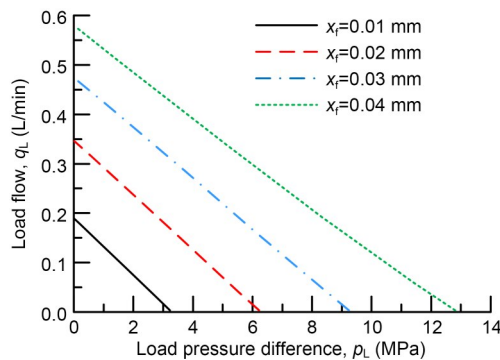
Fig. 10 Calculation process of static characteristics

3.1 Pressure-flow characteristics

The pressure-flow characteristics refer to the relationship between the load pressure difference p_L between the two chambers and the load flow q_L through the two chambers under different deflector positions. These are the most important static characteristics of the pilot stage. As shown in Fig. 11, it can be found that when the deflector is fixed, there is an approximate linear relationship between the load flow and the load pressure; the flow-pressure coefficient is constant. When the load pressure increases, the load flow basically decreases linearly.

Table 1 Structure parameters and empirical constants

Parameter	Value
Width of jet nozzle, a (mm)	0.155
Thickness of jet-pan, b (mm)	0.51
Distance from jet nozzle to receiving chamber, D (mm)	1.04
Thickness of the deflector, d (mm)	0.6
Width of guide groove outlet, a_n (mm)	0.123
Half angle of guide groove, θ ($^\circ$)	18.35
Length of receiving chamber, L_r (mm)	0.221
Width of the wedge, e (mm)	0.1
Energy loss coefficient, ζ_1	0.09
Entrainment coefficient, λ	0.435
Pressure constant, p_a (MPa)	3.5
Supply pressure, p_s (MPa)	21
Return pressure, p_t (MPa)	0
Flow coefficient, C_d	0.85
Oil density, ρ (kg/m^3)	778
Oil dynamic viscosity, μ ($\text{Pa}\cdot\text{s}$)	1.14×10^{-3}

**Fig. 11 Pressure-flow characteristics of the pilot stage at different positions**

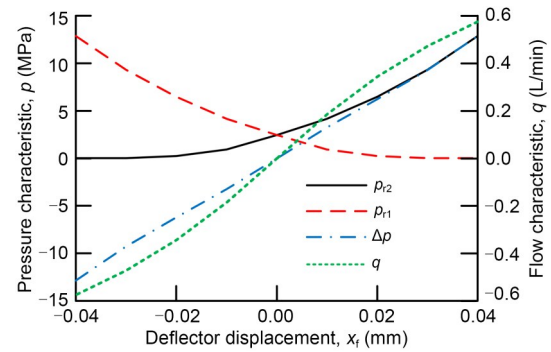
3.2 Cut-off load pressure characteristics

When the load flow drops to zero, the load pressure difference p_L between the two chambers is the cut-off load pressure Δp . The cut-off load pressure reflects the maximum load capacity that can be achieved by the pilot stage. It can be seen from Fig. 12 that with the increase of the deflector position, the pressure of the high-pressure chamber increases more obviously, while the pressure of the low-pressure chamber decreases and tends to be flat. The pressure difference is approximately linear with the deflector position.

3.3 No-load flow characteristics

When the load pressure decreases to zero, the load flow q_L is the no-load flow between the two

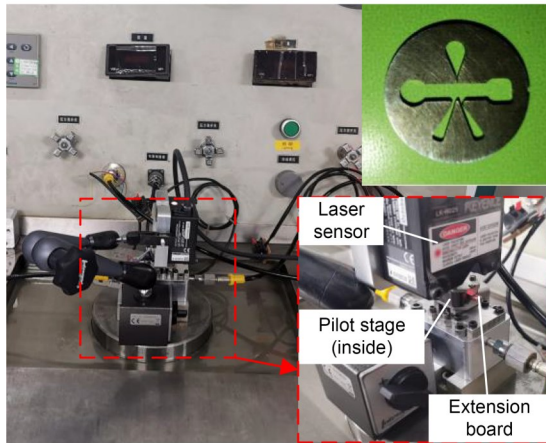
chambers. The no-load flow reflects the response speed of the pilot stage. The higher the no-load flow is, the faster the response speed of the pilot stage is. It can be found from Fig. 12 that with the increase of the deflector position, the no-load flow increases gradually, but the flow gain gradually decreases.

**Fig. 12 Pressure characteristics and flow characteristics of the pilot stage**

4 Model verification and discussion

4.1 Pressure characteristics test

The pilot stage cut-off load pressure characteristics experiment of a DJSV was carried out on the test rig as shown in Fig. 13a by the Aviation Key Laboratory of Science and Technology on Aero Electromechanical System Integration, China, and the main structure parameters of the pilot stage are shown in Fig. 13b and are consistent with those in Table 1. The medium is RP3 fuel, and the temperature is 17–20 $^\circ\text{C}$. The return pressure p_t is zero, the supply pressures p_s are 1, 5, and 10 MPa, respectively. The experimental principle is shown in Fig. 14. In the experiment, different control currents Δi are applied to the torque motor, the armature displacement is measured by the laser displacement sensor (LK-H025 Series, KEYENCE, Japan, with measurement resolution of 0.01 μm), and the recovery pressures of the receiving chambers are measured by a pressure gauge with measurement resolution of 0.01 MPa. To facilitate the measurement of the armature displacement, an extension board is attached to the armature. The deflector displacement can be obtained indirectly by the geometric relation of the armature components. Experimental data of deflector displacement and cut-off load pressure under different supply pressures are shown in Table 2.



(a)



(b)

Fig. 13 Experimental setup: (a) test rig; (b) jet-pan of pilot stage

The load pressures under different supply pressures are non-dimensionalized and compared with the theoretical model results, as shown in Fig. 15. It can be found from experimental data that when the deflector displacement is small, the dimensionless pressures under different supply pressures are close to each other, while, when the deflector displacement is large, the increase of supply pressure makes the dimensionless pressure increase slightly. The model calculation

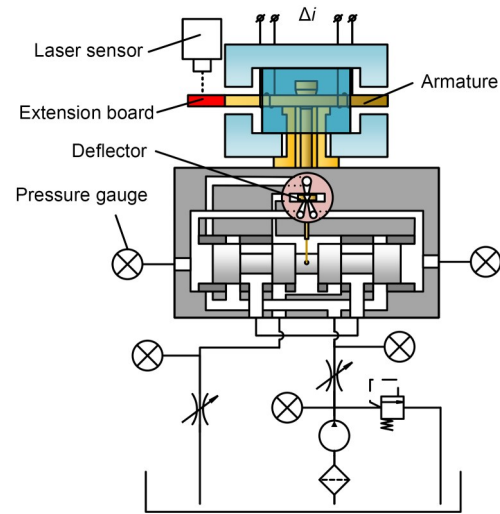


Fig. 14 Schematic diagram of experimental setup

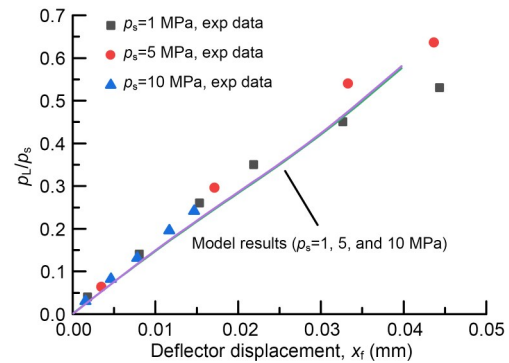


Fig. 15 Dimensional cut-off load pressure characteristics

also shows that there is little difference in the dimensionless pressure characteristics under different supply pressures. The model results are in good agreement with the experimental results, which indicates the reliability of the mathematical model of the pilot stage.

It is worth mentioning that, by modifying the parameters of the 2D mathematical model, a better fitting effect can be achieved for the static characteristics

Table 2 Relationship between cut-off load pressure and deflector displacement under different supply pressures

$p_s=1$ MPa		$p_s=5$ MPa		$p_s=10$ MPa	
Deflector displacement, x_f (μm)	Cut-off load pressure, p_L (MPa)	Deflector displacement, x_f (μm)	Cut-off load pressure, p_L (MPa)	Deflector displacement, x_f (μm)	Cut-off load pressure, p_L (MPa)
1.80	0.04	3.49	0.32	1.54	0.30
8.09	0.14	17.14	1.48	4.65	0.82
15.32	0.26	33.27	2.70	7.81	1.31
21.89	0.35	43.67	3.18	11.70	1.96
32.67	0.45			14.69	2.41
44.34	0.53				

of a specific structure. However, because the flow in the third direction is ignored, the 2D model has some shortcomings in describing the flow field structure and in variable parameter analysis.

4.2 Validation of the internal flow field model

In addition to the static characteristics, the internal flow law is another important indicator reflecting the accuracy of the model. However, as the structural size of the pilot stage is too small (less than 1 mm), it is difficult to carry out a flow field visualization test, so this part is verified by finite element analysis (FEA). As shown in Fig. 16, a 3D flow field simulation model for the pilot stage of DJSV is established. In the model, a thin-walled orifice is used to simulate the load between two chambers, and orifices with different diameters can simulate the influence of different loads on the flow field. The velocity distribution of 3D jets in the free jet region and the jet entrainment in the pressure recovery region are verified in this part.

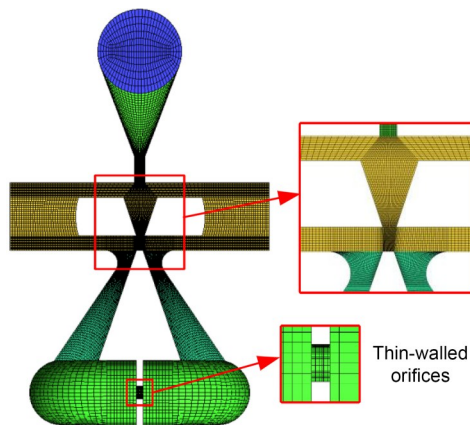


Fig. 16 Schematic diagram of the experimental setup

4.2.1 Verification of the 3D jet model

The velocity distribution in the streamwise direction at section 2-2 of the deflector at 0 and 0.04 mm in the free jet region are compared based on the FEA result (Fig. 17a) and the model result (Fig. 17b). In this FEA case, the diameter of the damping orifice is zero, and the velocity distributions in the free jet area under different loads are almost the same. It can be found that the jets expand in both the x direction and the y direction. In addition, it is not difficult to find that the shape of the isovelocity line in the flow field is close to the shape of a straight slot, which is similar

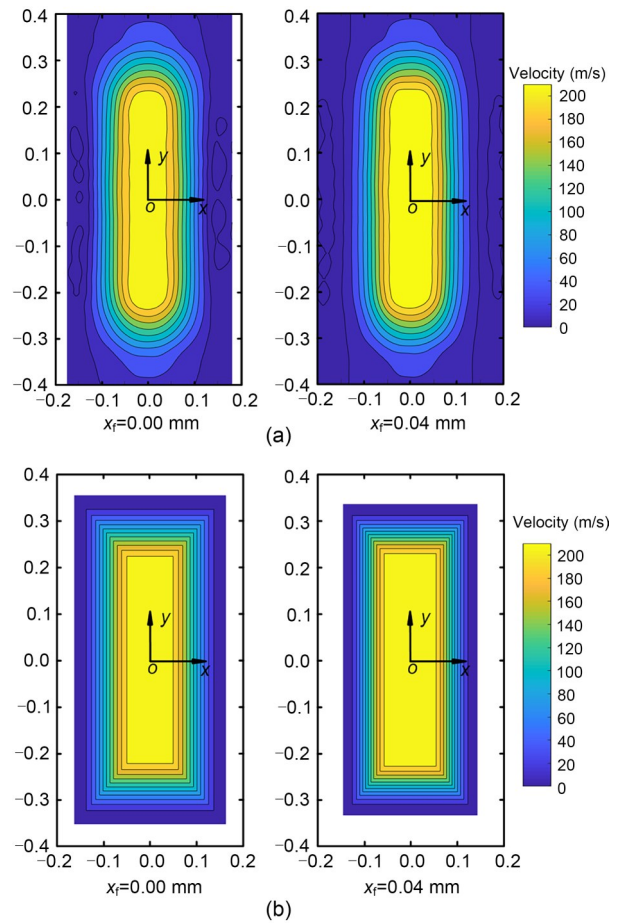


Fig. 17 Velocity distribution along the streamwise direction at section 2-2: (a) FEA result; (b) model result

to the shape of the rectangular isovelocity line proposed in this study. The higher the velocity is, the more obvious is the rectangular feature of the isovelocity line. With the offset of the deflector, the range of the constant velocity region expands, and the width of the shear layer decreases. These characteristics are consistent with the 3D turbulent jet model proposed in this study.

4.2.2 Jet entrainment in the receiving chamber

Fig. 18 shows the velocity of the pilot stage flow field. Taking the right receiving chamber as an example, it can be seen that the jet lengths of a secondary jet entering the receiving chamber are not the same under different working conditions.

In Fig. 18a, the deflector position is 0.04 mm, the diameters of the damping orifices D_o are 0.5 and 0.1 mm, respectively, and the recovery pressures of the right receiving chamber are 2.74 and 9.24 MPa,

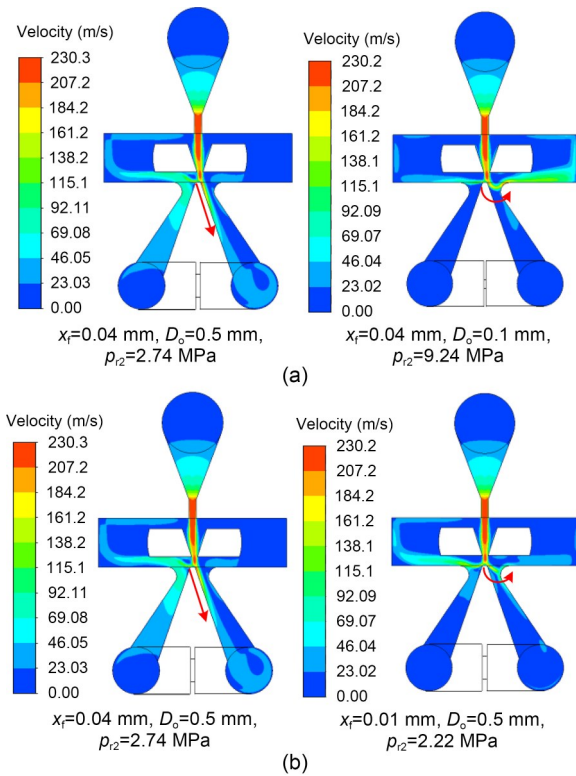


Fig. 18 Jet entrainment in receiving chamber: (a) flow field under different orifices; (b) flow field under different deflector positions

respectively in the two cases. It can be found that although the deflector position is the same, the jet length is affected by the recovery pressure of the receiving chamber; the increase of pressure leads to the shortening of jet length and the reduction of entrainment flow.

Fig. 18b shows the flow field when the deflector positions are 0.04 and 0.01 mm, the diameter of the damping orifice D_o is 0.5 mm, and the recovery pressures of the right receiving chamber are 2.74 and 2.22 MPa, respectively. It can be found that although the recovery pressure is smaller when the deflector is 0.01 mm, the jet length is still shorter due to the smaller secondary jet flow rate into the receiving chamber. Therefore, the secondary jet flow rate into the receiving chamber is another important factor related to entrainment flow rate.

In this section, some regular explorations have been made on jet entrainment in the pressure recovery region, and the parameters in Eq. (22) are obtained through parameter fitting. In fact, jet entrainment is very complex and affected by many factors, and a more accurate jet entrainment model is worth further exploration.

5 Conclusions

1. The flow law of the pilot stage of flow field of the DJSV is revealed and a new flow field mathematic model for the pilot stage of the DJSV is established based on a 3D jet model and a jet entrainment model. The process of fluid energy transfer and the working principle of the pilot stage are clarified. Compared with the traditional 2D mathematical model, the 3D mathematical model reflects the flow field structure of the pilot stage more accurately. In particular, it is advantageous in analyzing the static performance when the structural parameters change.

2. The expression of velocity distribution in a 3D free jet region is presented; the isovelocity line in the streamwise direction is rectangular. In the pressure recovery region, the coupling relationship between jets flow rate and recovery pressure is established, and the jet entrainment model is put forward to overcome the problem of low calculation of recovery pressure.

3. The pressure-flow characteristics, pressure characteristics, and flow characteristics of the pilot stage are derived. The pressure characteristics of the pilot stage are tested and the results show that the dimensionless cut-off load pressure characteristics are basically the same under different supply pressures. The experimental results are in agreement with the theoretical results. The 3D mathematical model is beneficial for the structural improvement of the pilot stage.

Acknowledgments

This work is supported by the National Natural Science Foundation of China (Nos. 51775383 and 52175059).

Author contributions

Jia-yang YUAN and Sheng-rong GUO designed the research. Shuang-lu LI processed the corresponding data and wrote the first draft of the manuscript. Yao-bao YIN helped to organize the manuscript and revised and edited the final version.

Conflict of interest

Shuang-lu LI, Yao-bao YIN, Jia-yang YUAN, and Sheng-rong GUO declare that they have no conflict of interest.

References

- Karunanidhi S, Singaperumal M, 2010. Mathematical modeling and experimental characterization of a high dynamic servo valve integrated with piezoelectric actuator. *Proceedings of the Institution of Mechanical Engineers, Part I: Journal of Systems and Control Engineering*, 224(4):

- 419-435.
<https://doi.org/10.1243/09596518JSCE899>
- Li YS, 2016. Mathematical modelling and characteristics of the pilot valve applied to a jet-pipe/deflector-jet servo-valve. *Sensors and Actuators A: Physical*, 245:150-159.
<https://doi.org/10.1016/j.sna.2016.04.048>
- Liu XQ, Ji H, Min W, et al., 2020. Erosion behavior and influence of solid particles in hydraulic spool valve without notches. *Engineering Failure Analysis*, 108:104262.
<https://doi.org/10.1016/j.engfailanal.2019.104262>
- Liu YS, Dong J, Wu S, et al., 2019. Theoretical research on the dynamic characteristics of electrohydraulic servo valve (EHSV) in deep sea environment. *Ocean Engineering*, 192:105957.
<https://doi.org/10.1016/j.oceaneng.2019.04.038>
- Marsters GF, 1981. Spanwise velocity distributions in jets from rectangular slots. *AIAA Journal*, 19(2):148-152.
<https://doi.org/10.2514/3.50935>
- Saha BK, Li SJ, Lv XB, 2020a. Analysis of pressure characteristics under laminar and turbulent flow states inside the pilot stage of a deflection flapper servo-valve: mathematical modeling with CFD study and experimental validation. *Chinese Journal of Aeronautics*, 33(3):1107-1118.
<https://doi.org/10.1016/j.cja.2019.11.016>
- Saha BK, Peng JH, Li SJ, 2020b. Numerical and experimental investigations of cavitation phenomena inside the pilot stage of the deflector jet servo-valve. *IEEE Access*, 8: 64238-64249.
<https://doi.org/10.1109/ACCESS.2020.2984481>
- Sangiah DK, Plummer AR, Bowen CR, et al., 2013. A novel piezohydraulic aerospace servovalve. Part 1: design and modelling. *Proceedings of the Institution of Mechanical Engineers, Part I: Journal of Systems and Control Engineering*, 227(4):371-389.
<https://doi.org/10.1177/0959651813478288>
- Sforza PM, Steiger MH, Trentacoste N, 1966. Studies on three-dimensional viscous jets. *AIAA Journal*, 4(5):800-806.
<https://doi.org/10.2514/3.3549>
- Squire HB, Trouncer J, 1944. Round Jets in a General Stream. Aeronautical Research Council, Reports and Memoranda No. 1974, London, UK.
- Stefanski F, Minorowicz B, Persson J, et al., 2017. Non-linear control of a hydraulic piezo-valve using a generalised Prandtl-Ishlinskii hysteresis model. *Mechanical Systems and Signal Processing*, 82:412-431.
<https://doi.org/10.1016/j.ymsp.2016.05.032>
- Tamburrano P, Plummer AR, Distaso E, et al., 2018. A review of electro-hydraulic servovalve research and development. *International Journal of Fluid Power*, 20(1):53-98.
<https://doi.org/10.13052/ijfp1439-9776.2013>
- Tamburrano P, Plummer AR, de Palma P, et al., 2020. A novel servovalve pilot stage actuated by a piezo-electric ring bender: a numerical and experimental analysis. *Energies*, 13(3):671.
- Yan H, Ren YK, Yao L, et al., 2019. Analysis of the internal characteristics of a deflector jet servo valve. *Chinese Journal of Mechanical Engineering*, 32(2):31.
<https://doi.org/10.1186/s10033-019-0345-7>
- Yin YB, Yuan JY, Guo SR, 2017. Numerical study of solid particle erosion in hydraulic spool valves. *Wear*, 392-393: 174-189.
<https://doi.org/10.1016/j.wear.2017.09.021>
- Yin YB, Li SL, Zhang XW, et al., 2019. Steady-state flow force calculation of the first stage in a deflector jet servo valve. IEEE 8th International Conference on Fluid Power and Mechatronics, p.452-458.
<https://doi.org/10.1109/FPM45753.2019.9035735>
- Zheng FX, Li S, Ding C, et al., 2021. Theoretical and experimental research on the cartridge two-dimensional (2D) electro-hydraulic servo valve. *Advances in Mechanical Engineering*, 13(2):168781402199653.
<https://doi.org/10.1177/1687814021996532>
- Zhu MZ, Zhao SD, Dong P, et al., 2018. Design and analysis of a novel double-servo direct drive rotary valve with high frequency. *Journal of Mechanical Science and Technology*, 32(9):4313-4323.
<https://doi.org/10.1007/s12206-018-0829-x>